Acoustic properties in travertines and their relation to porosity and pore types

J. Soete [a, *], L.M. Kleipool [b], H. Claes [a], S. Claes [a], H. Hamaekers [a, f], S. Kele [c, d], M. Özkul [e], A. Foubert [f], J.J.G. Reijmer [b], R. Swennen [a]

[a] Geology, Department of Earth and Environmental Sciences, KU Leuven, Celestijnenlaan 200E, B-3001 Heverlee, Belgium
[b] Sedimentology and Marine Geology, Faculty of Earth and Life Sciences, VU University Amsterdam, De Boelelaan 1085, 1081 HV Amsterdam, The Netherlands
[c] Institute for Geochemical Research, Hungarian Academy of Sciences, Budaörsi út 45, 1112 Budapest, Hungary
[d] ETH Zürich, Sonneggstrasse 5, 8092 Zürich, Switzerland
[e] Department of Geological Engineering, Pamukkale University, TR−20070 Denizli, Turkey
[f] Department of Geosciences, Université de Fribourg, Chemin du Musée 6, 1700 Fribourg, Switzerland

Sonic velocities of Pleistocene travertines were measured under variable confining pressures. Combined with petrographical characteristics and petrophysical data, i.e. porosity, permeability and density, it was determined that travertine porosity, pore types and cementation control compressional-wave (V_p) and shear-wave velocity (V_s). At 40 MPa confining pressures, V_p ranges between 3695 and 6097 m/s and V_s between 2037 and 3140 m/s. Velocity variations in travertines are, as with all carbonates, primarily linked to sample heterogeneity, i.e. differences in fabric, texture and porosity. They thus not necessarily emanate from changes in mineralogy or composition. Body wave velocities have a positive correlation with sample density and an inverse correlation with porosity. The travertines, sampled in extensional settings with normal faulting activity, define a specific compressional-wave velocity (y-axis) versus porosity (x-axis) equation, i.e. ($\log(y) = -0.0048x + 3.7844$) that differs from the V_p-porosity paths defined by marine carbonates. Acoustic wave velocities are higher for travertines than for marine carbonates. Travertine precipitates form rigid rock frames, often called framestone, with large primary pores. Marine carbonates on the other hand often consist of (cemented) transported sediments, resulting in a rock frame that permits slower wave propagation when compared to the continental limestones.

Acoustic velocity variations are linked to variations in pore types. Mouldic pores (macropores) show faster wave propagation than expected from their total porosities. Microporosity, interlaminar and interpeloidal porosity result in slower acoustic velocities. Framework pores and micro-moulds are associated with lowered acoustic velocities, while vug porosity is found above, on and below the general velocity-porosity trend. Not only the pore type, but also pore shapes exert control on body wave velocities. Cuboid-and rod-like pore shapes increase the velocity, while plate-and blade-like pore shapes have a negative effect on the velocity. The study demonstrates how seismic sections in travertine systems can contain seismic reflections that are not caused by non-carbonate intercalations, but relate to geobody boundaries, in which the seismic expression is function of porosity, pore types and shapes. This study provides and relates petrophysical data, i.e. porosity, permeability and acoustic velocities of travertines and is of importance for the interpretation of seismic reflection data in subsurface continental carbonate reservoirs.

1. Introduction

Carbonate deposits gained interest due to their potential as reservoir rocks, e.g. the supergiant fields in the Middle East (Nurmi and Standen, 1997) and offshore Brazil (Thompson and Oftebro, 2011; Wright, 2012). The genesis of continental carbonates is associated with physico-chemical and biological precipitation that

* Corresponding author. Tel.: +32 16 32 77 96.
E-mail address: jeroen.soete@ees.kuleuven.be (J. Soete).

largely influences the rock texture and petrophysical properties (Toumelin et al., 2003). This causes petrophysical heterogeneity that can become even more pronounced due to diagenetic over-printing (with cementation, dissolution, recrystallisation, dolomitisation, fracturing, etc.). The studied continental carbonates in Turkey and Hungary are calcareous spring deposits, i.e. travertines (Pentecost, 2005), associated with ambient and hydrothermal fluids (El Desouky et al., 2014; Sierralta et al., 2010). Their deposition is controlled by a complex interplay of physico-chemical, biological and hydrological factors, including CO_2 degassing, the dominating process for travertine precipitation (Fouke, 2011; Guo and Riding, 1998; Kele et al., 2011; Özkul et al., 2013, 2014; Pentecost, 2005). Travertines can form in a thin water film in sub-aerial conditions, or in lake, marsh and fluvial environments. These precipitates have been widely studied (Alonso-Zarza and Tanner, 2010; Ford and Pedley, 1996; Pedley and Rogerson, 2010; Pentecost, 2005), however, a detailed investigation of the rock petrophysics was seldom accomplished. This paper aims to investigate the behaviour of acoustic waves in travertines.

The dependency of sonic velocities on lithology, rock texture and fabric is the key to understand acoustic logs and seismic sections in sedimentary systems. Compressional-wave velocity and bulk density are used to calculate acoustic impedance. In carbonate lithologies that consist purely of calcite, grain density variations are limited, meaning that other parameters cause variations in body wave velocity. These parameters are of importance for the interpretation of seismic reflection and geophysical data. The control that is exhibited by porosity on acoustic velocity was already reported in the late fifties (Biot, 1956; Gassmann, 1951). Causes for velocity variations in pure carbonates were part of several studies especially from the early nineties onwards. It was concluded that not only porosity, but also the entire rock fabric and its texture are of importance (Anselmetti and Eberli, 1993; Wang et al., 1991). Moreover, carbonates are prone to diagenesis, which can easily alter porosity, crystal morphology, the rigidity of the solid framework, etc. (Anselmetti and Eberli, 1993; Braaksma et al., 2003; Verwer et al., 2008).

In this study, compressional-wave velocity (V_p) and shear-wave velocity (V_s) are measured on travertine samples from three different locations, under confining pressures that approach in situ subsurface conditions. Sonic velocity measurements were done in combination with petrography, X-Ray Diffraction (XRD) and micro-Computer Tomography (μCT) analyses.

2. Geological setting

The selected dataset of Quaternary travertines is assembled from quarries near Denizli, in Turkey (Özkul et al., 2013) and from Süttő (Bakacsi et al., 1994; Sierralta et al., 2010) and Budakalász (Kele et al., 2003) in Hungary.

The Denizli Basin (Western Turkey) is a Neogene-Quaternary depression, of 70 by 50 km. The basin is the continuation of the E−W-trending Büyük Menderes Graben and the NW−SE-trending Gediz Graben (Bozkurt and Bozkurt, 2009; Gürer and Yilmaz, 2002; Kele et al., 2011; Özkul et al., 2002, 2013). The Quaternary deposits are subdivided in the Tosunlar Formation, with alternating conglomerate, sand- and mudstone deposits, and alluvial fans of the uppermost Quaternary. The alluvium strata are associated with travertines (Alçiçek et al., 2007). The travertine deposits examined in this study are situated in the Ballık area, at the junction of the locally E−W-trending Denizli Graben and the adjacent NW−SE-trending Baklan Graben (Gürbüz et al., 2012; Van Noten et al., 2013). The sampling location for this study is the Alimoğlu quarry.

The Transdanubian Range (TR) is a horst structure in the Pannonian Basin, Hungary (Dolton, 2006; Haas, 2012). The Buda Mountains and Gerecse Hills crop out along the Danube River. They are part of the Transdanubian Range and are mainly comprised of Mesozoic carbonates, which are covered by Cenozoic clastic and carbonate sequences. The terrace region of the Danube River is characterised by alluvial deposits (sand and gravel), but often travertine precipitates exist. The Budakalász and Süttő travertines, respectively from the Buda Mountains and Gerecse Hills are examples of deposits that cover geomorphic steps (terraces) of the Danube River.

Travertines (including the world heritage site of Pamukkale) are known to occur along basin bounding normal faults. Meteoric water infiltrates along topographically elevated areas, such as horst structures (Mehmet Özkul et al., 2013). Above average geothermal gradients, associated with extensional settings and volcanic activity, are two important factors steering infiltrated and thermal waters. Meteoric water can mix with for example karstic water, and form corrosive fluids that enhance carbonate dissolution. Strontium isotope analyses, both on bulk samples and crystalline cement bands have shown that the Lycian nappes (Mesozoic) are a likely candidate as source rock in the Ballık area (El Desouky et al., 2014; Gündoğan et al., 2008; Kele et al., 2011). Surfacing along normal faults of CO_2-rich, thermal fluids results in the precipitation of travertines (Goldscheider et al., 2010; Nador, 1993; Sierralta et al., 2010).

3. Methodology

The petrophysical measurements are conducted on sixty 1.5-inch (3.81 cm) diameter plugs. The effective porosity in the plugs is measured by means of helium expansion porosimetry. Gas permeability, in this case with nitrogen gas (N_2), is measured in a steady state permeameter.

XRD analyses were conducted on 10 representative samples to confirm that travertines in Denizli and from Süttő and Budakalász are composed for well over 90% of calcite, as previously stated in several studies (Kele, 2009; Kele et al., 2011; Khatib et al., 2014; Özkul et al., 2013; Sierralta et al., 2010). Measurements have been carried out at 45 kV and 30 mA, using Cu-Kα-radiation and a scan speed of 0.010° 2θ/s. Diffraction patterns are subsequently compared against mineral patterns of a standard database in the DIFFRAC^{plus}, 2004, EVA software 10.0 rev. 1 (Bruker, 2013). Quantitative analyses are carried out using the Rietveld method, with TOPAS-Academic V4.1 and JEdit V4.2 software packages (Coelho, 2012).

Prior to the sonic velocity analysis, the plugs are dried at 65 °C for at least three days to ensure that all water is removed from the samples. Even small amounts of water could significantly lower the elastic shear moduli and give cause to erroneous analyses data (Mavko et al., 2009). Next, samples are left to equilibrate for 48 h at room temperature and humidity conditions (19−21 °C, 50−60%). Ultrasonic compressional-wave velocity (V_p) and shear-wave velocity (V_s) are measured with a High Pressure (ultrasonic) Measurement System (HPMS), as function of the applied confining pressure with a transducer arrangement (VerdeGeoscience©, Vermont, U.S.A.) that propagates one compressional and two independent and orthogonally shear waves (V_s1 and V_s2) along the core axis. The orthogonal shear-waves are averaged to produce a homogeneous shear-wave velocity. The experimental setup contains a source and receiver crystal. The source crystal is excited by a fast rise time electrical voltage pulse, producing a sonic pulse with a frequency of 1 MHz. The receiver crystal records the flight-time of the first arriving wave front of the sonic pulse (García-del-Cura et al., 2012).

Acoustic velocities are obtained by measuring the one-way travel time along the sample axis divided by the sample length. The arrival time is picked when the signal exceeds a threshold of the first three half-cycles of the signal. The error range of the ultrasonic velocity measurements falls within 3%. The measurements were conducted at confining pressures of 2.5, 5, 10, 20 and 40 MPa in a hysteresis loop.
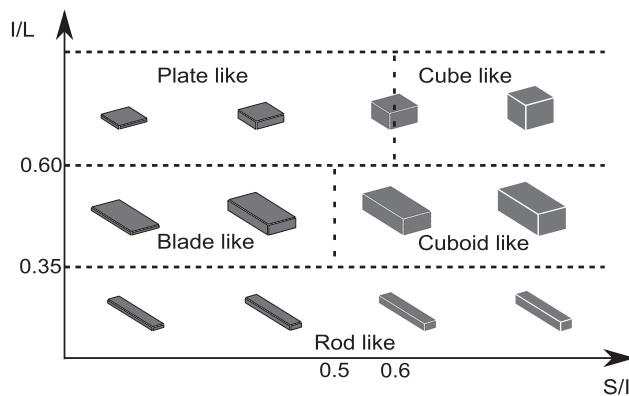
The elastic moduli can be extracted from the velocity measurements and the sample density (Mavko et al., 2009). The density of the plugs, both dry and bulk, are calculated from the dry and saturated weights in combination with the cylindrical volume. The grain density of the samples is determined with a Micromeritics Accupyc 1330 helium pycnometer and porosity (error-range of 1%) is subsequently calculated from dry and grain density (Anselmetti and Eberli, 1993; Kenter et al., 1997; Verwer et al., 2008).

Thin section and Scanning Electron Microscopy (SEM) were executed to determine dominant pore types in each sample. In addition, ten representative samples were scanned with μCT to render the pore network in 3D and to describe the pore network into artificial three-dimensional shapes. The μCT is a Phoenix Nanotom S machine (GE Measurement and Control Solutions, Wunstorf, Germany), equipped with a 180 kV/15 W high-performance nanofocus X-ray tube and a 2304 × 2304 pixel Hamamatsu detector. A voltage of 140 kV and current of 280 μA is applied to a tungsten target. A 0.3 mm thick cupper filter is installed during the scans. Radiographs are reconstructed with the Phoenix datos|x 2.0 reconstruction software (GE Measurement and Control Solutions, Wunstorf, Germany) and images with an isotropic voxel size of 16 μm^3 are exported. The slices are segmented and analysed in Matlab R2011b, J-MicroVision (Roduit, 2002, 2007) and Avizo Fire v.7 software. Pore shape parameters such as sphericity, compactness and form ratio (with 'L', assigned to the longest dimension of the pore, the parameter 'I' assigned to the longest dimension perpendicular to L and 'S' orthogonal to both L and I) are calculated based on the segmented CT images (Claes et al., 2013). The combination of several shape indices provides the best method of grouping and discriminating between 3D shapes (Blott and Pye, 2008). The described shape is considered a good approach for a pore if the ellipsoid volume (E_v), with semi-principal axes equal to respectively I, L and S, and the pore object volume (P_v) ratio is close to one. A watershed method is introduced that splits up pore objects for which E_v/P_v does not fall between 0.5 and 1.5. The pore shape parameters are then calculated for the newly created sub-pores. A pore shape classification system (Fig. 1) based on the results of this analysis and the particle classification system of Blott and Pye (2008) is proposed to investigate the influence of pore shape on body wave velocities.

4. Results

4.1. Mineralogy

The analysed travertines consist of over 94% of calcite. Next to the dominant carbonate mineralogy, a minor presence of quartz can be deduced. Except for quartz, small amounts of amorphous phases, organic matter and clays occur in some of the samples (Fig. 2). The amorphous phase cannot be analysed with XRD and the exact mineralogy of the minor quantities of clay minerals is beyond the scope of this study. Aragonite is observed in travertines around the world (Pentecost, 2005), but is absent in the analysed samples. The analyses confirmed that travertines from the examined quarries are calcite dominated (≥94%) as previously stated in several studies (Kele, 2009; Kele et al., 2011; Khatib et al., 2014; Özkul et al., 2013; Sierralta et al., 2010).

4.2. Petrography

The dataset can be subdivided petrographically into 7 dominant pore types: (1) microporosity, (2) interpeloidal porosity (3) interlaminar porosity, (4) mouldic porosity, (5) micro-mouldic porosity, (6) vuggy porosity and (7) framework porosity. Calculating the equivalent circular pore diameter approached the pore size.

Microporosity (<10 μm) and interlaminar porosity dominate samples with less than 10% porosity. **Microporosity** is mainly found in between micritic particles and structures (Fig. 3A). **Interlaminar porosity** (Fig. 3B) is found in the vicinity of dendritic crusts (Fig. 3C) and occurs below these crusts. This is likely the result of encrustation of algae and/or bryophytes, or possibly other organic components and their subsequent decay. The desiccation of dendritic layers can cause shrinkage and will induce interlaminar porosity. Interlaminar pores range between 10 μm and a few centimetres. Peloids are important building components in travertine rocks. **Interpeloidal porosity** (Fig. 3D), produced by the formation of a peloidal framework, often follows lamination on macroscale and because of their intergranular nature, they are referred to as pseudo-fenestrae (Flügel, 2010). Interpeloidal pores have diameters from 10 μm to 500 μm. **Moulds** are associated with plant (macrophyte, bryophyte), relict-algae content and possibly associated former microbial activity. Mouldic and micro-mouldic porosity are formed by the calcite encrustation and subsequent decay of the organic matter. The moulds are thus secondary in origin. Mouldic pores have equivalent circular diameters that start at mm scale, but go up to several cm. **Micro-moulds** are mouldic pores smaller than 500 μm. The pore space is often surrounded by a rigid micritic frame, consisting of dendritic crusts (Fig. 4A) or peloids (Fig. 4B). Isopachous rims of bladed to dogtooth cements often reduce the mouldic pore space. **Vuggy** porosity in this article follows the definition of Choquette and Pray (1970) and Lønøy (2006). Vuggy pores (Fig. 4C) are non-fabric selective secondary solution pores. Vugs encountered in the travertines are very often solution-enlarged interpeloidal and mouldic pores. The pores can be recognized by the rounded edges that cut across crystal and grain boundaries. Vuggy pores have the largest range in pore size, which can occur from μm to dm sized. **Framework Porosity** (Fig. 4D) is formed between a complex network of interfingering overcrusted former plants (bryo- and macrophytes) and other forms of organic matter. In a thin section this pore type looks like an assemblage of mouldic porosity (Fig. 4E and F). Another way to achieve porosities of over 30% is through the initiation of diagenetic processes (dissolution, pedogenesis, etc.).

4.3. Petrophysical properties

Sixty travertine plugs were analysed to assess the impact of porosity, pore types and shapes on body wave propagation. Measured values of the dry density (ρ_d), grain density (ρ_g), porosity, Klinkenberg permeability, P-wave velocity, S-wave velocity and acoustic impedance data are given in Table 1. ρ_d and ρ_g range from 1.77 to 2.57 g/cm^3 and 2.56 to 2.72 g/cm^3 respectively. Grain density variations in continental carbonates are associated with
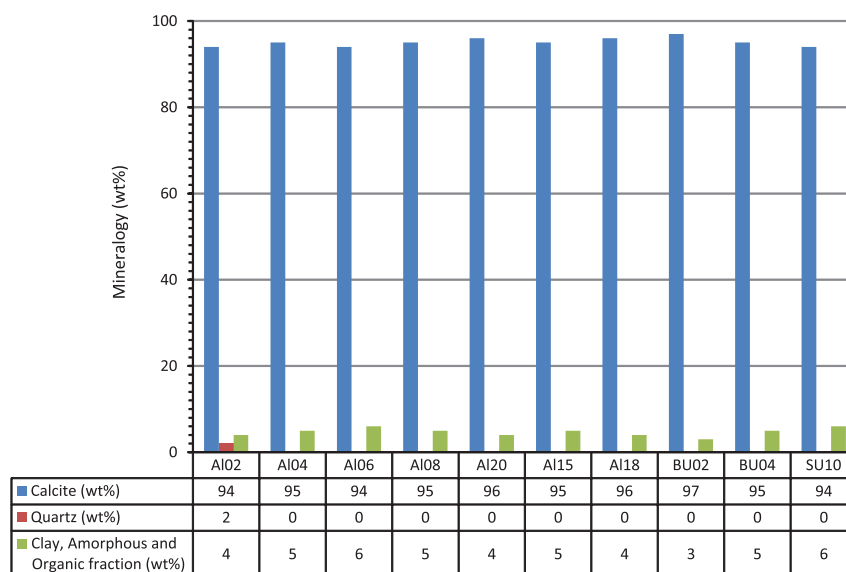
Figure 1. Pore type classification based on the ratios of the longest (L), intermediate (I) and shortest (S) pore dimensions.

	Al02	Al04	Al06	Al08	Al20	Al15	Al18	BU02	BU04	SU10
■ Calcite (wt%)	94	95	94	95	96	95	96	97	95	94
■ Quartz (wt%)	2	0	0	0	0	0	0	0	0	0
■ Clay, Amorphous and Organic fraction (wt%)	4	5	6	5	4	5	4	3	5	6

Figure 2. Mineralogical composition (wt%) of the travertine samples, determined with XRD.

alternations in fabrics with, for example, more dense sparite crystals when compared to micritic fabrics (Pentecost, 2005). The samples yield porosity values of 2.8−34.7% (mean value of 12.9%). The nearly perfect correlation, with a correlation coefficient of 0.99, between different porosity methods confirms the consistency of the individual measurements. Permeability data (Fig. 5) of the carbonates show a skewed distribution and a large range over several orders of magnitude, between 0.05 and 18 000 mD. Carbonates, heterogeneous with complex primary fabrics and prone to diagenetic alteration (e.g. dissolution, cementation, recrystallisation, dolomitisation, etc.), generally contain complex pore networks that may complicate the relation between porosity and permeability parameters (Dewit et al., 2012; Lapponi et al., 2011; Nurmi and Standen, 1997). This effect is generally more
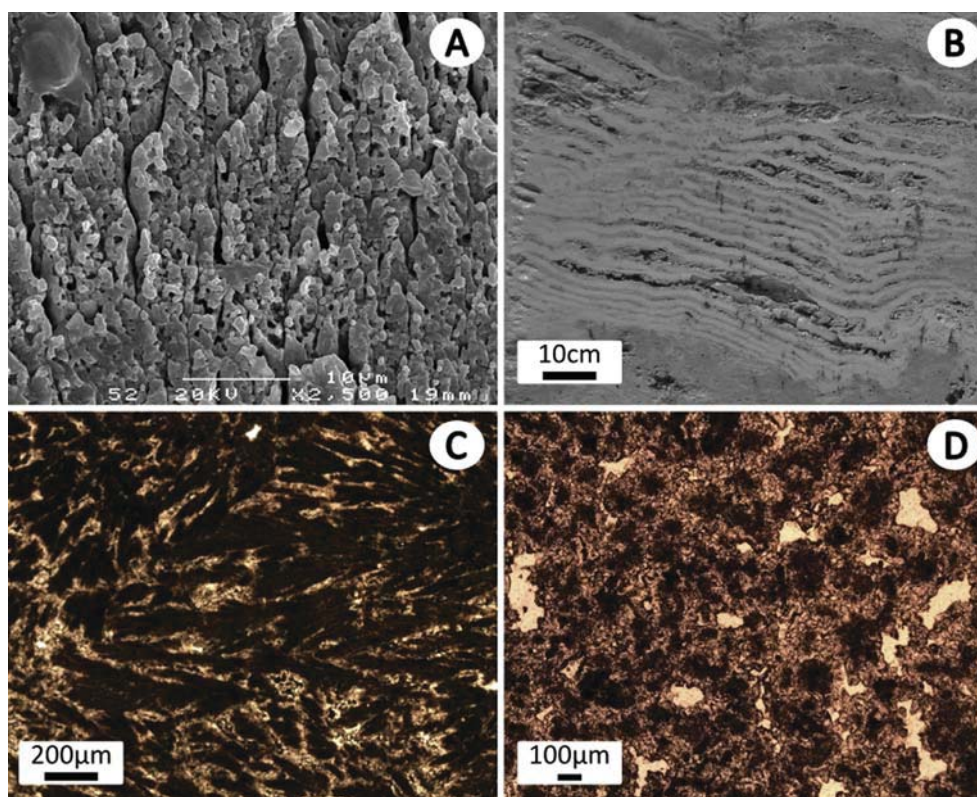

Figure 3. Macro-and microscopic images. (A) SEM photomicrograph of a micritic sample with micropores. (B) Interlaminar porosity between white dendritic crusts. (C) Microscopic image of a dendritic crust, formed by the intergrowth of dendrites. (D) Peloidal micrite (brown) with interpeloidal porosity and sparites (white). (For interpretation of the references to colour in this figure legend, the reader is referred to the web version of this article.)
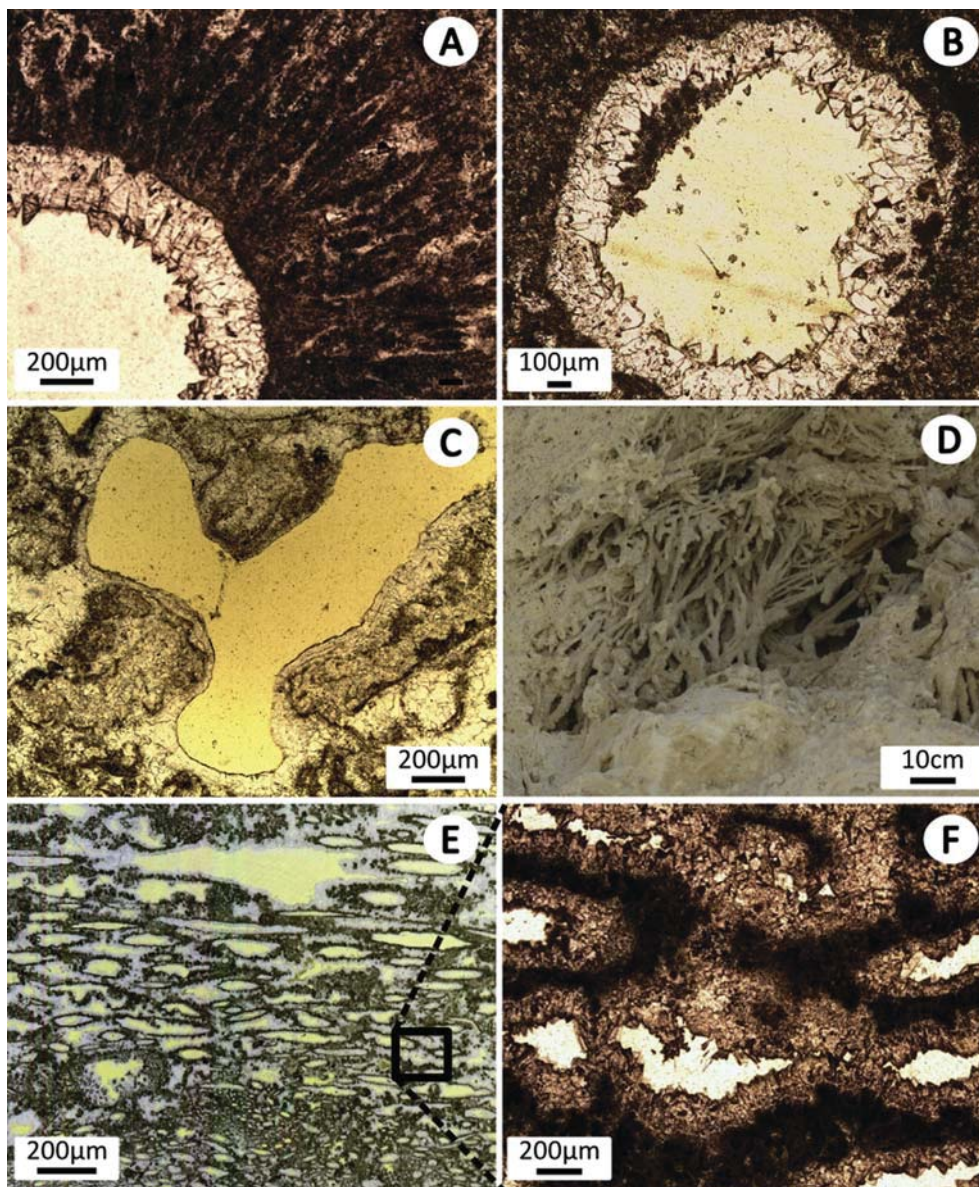
Figure 4. (A) Reed mouldic pore with dendrites that nucleate on the plant material, growing outward and sparites that reduce the pore space (after Claes et al., 2014). (B) Sparite reduced reed mould, surrounded by peloidal micrites. (C) Irregular vuggy pore, cutting through crystal and particle boundaries of surrounding peloidal micrites and sparites. (D) Framework porosity, formed by the encrustation of plant material. (E) Microscopic image of a framework porosity system and (F) zoom on sparite reduced reed moulds in the framework porosity system.

pronounced in continental carbonates, formed in a thin water film in sub-aerial conditions, with water supply from the spring, temperatures, humidity, etc. that are constantly changing.

4.4. Acoustic velocity measurements

Shear-wave velocity and compressional-wave velocity values are given for confining pressures of 40 MPa, which simulate in situ subsurface pressure conditions. The travertines display a wide range in velocities; V_p varies between 3695 and 6097 m/s, and V_s between 2037 and 3140 m/s. For a given sample, the V_s value is approximately 55% of the V_p value. The V_p versus V_p/V_s ratio plot (Fig. 6) is specifically included to show that V_p/V_s ratios range between 1.80 and 2. Hysteresis loops of the compressional-wave data illustrate, on the prograde path, an initial fast rise of the velocity, until a plateau is reached (in most cases around 10−20 MPa). At this point, instable micropores and microfractures are expected to close

(Anselmetti and Eberli, 1993) and their effect on the V_p data is minimized. Some of the samples show elastic deformation, approaching starting conditions towards the end of the hysteresis loop (Fig. 7, sample Al10). The retrograde path of most samples, however, is characterised by a slower velocity decrease with pressure than expected from the prograde path (Fig. 7, Al19). Compressional-wave velocities at the end of the analysis will be slightly higher than at starting conditions. The deformation inflicted during the prograde path is in this case non-elastic. Here, instable micro-fractures and pores likely remain closed after applying maximum pressures of 40 MPa. The edges of the samples are in some cases slightly affected. However, none of the retrograde paths show faster velocity decrease with pressure than observed in their prograde path, indicating that none of the samples disintegrated during the analyses.

Both compressional- and shear-wave velocities were plotted against Helium porosities (Fig. 8). Despite the fact that samples

5

Table 1
Summary of the conducted petrophysical measurements.

Sample	Facies	ρ_d (g/cc)	ρ_s (g/cc)	Accupyc φ (%)	Kl. Perm (mD)	V_p (40 Mpa) (m/s)	V_s (40 Mpa) (m/s)	A.I. (10^6 Ns/m^3)
Al01	Subh.	2.45	2.63	6.5	0.1	5440	2935	13.35
AL02	Subh.	2.49	2.63	5.2	0.2	5482	2968	13.68
Al03	Subh.	2.41	2.60	7.2	8.4	5619	2986	13.55
Al04	Subh.	2.50	2.57	2.8	0.1	5620	3012	14.03
Al05	Casc.	2.34	2.61	10.5	1.7	5420	2911	12.67
Al06	Wfall.	1.80	2.72	33.6	14 600	4075	2191	7.36
Al08	Reed	2.26	2.60	12.9	69.4	5628	2941	12.73
Al09	Reed	2.09	2.61	19.7	524	5253	2827	11.00
Al10	Subh.	2.37	2.62	9.7	0.1	5690	2998	13.49
Al11	Subh.	2.46	2.63	6.6	0.8	5710	3018	14.05
Al12	Subh.	2.46	2.65	7.2	0.1	5561	2988	13.66
Al13	Wfall.	1.94	2.66	26.8	1116	4267	2312	8.30
Al14	Wfall.	1.87	2.68	30.0	1611	4162	2182	7.80
Al15	Cascade	2.28	2.58	11.8	2.9	5071	2769	11.56
Al16	Cascade	2.31	2.57	10.3	0.2	4974	2735	11.49
Al17	Wfall.	2.28	2.66	14.2	8.3	4711	2605	10.74
Al18	Wfall.	2.11	2.65	20.4	10.3	4703	2557	9.91
Al19	Casc.	2.44	2.56	4.5	0.2	5663	2987	13.84
Al20	Casc.	2.37	2.58	8.3	1.0	5511	2952	13.05
SU01	Subh.	2.52	2.65	5.2	/	5670	3063	14.26
SU02	Reed	2.31	2.68	14.0	/	5283	2834	12.19
SU03	Subh.	2.53	2.66	5.1	/	5787	3070	14.63
SU04	Reed	2.34	2.69	13.0	/	5333	2859	12.48
SU05	Reed	1.80	2.71	33.5	/	3695	2037	6.65
SU06	Reed	1.77	2.71	34.7	/	3879	2149	6.86
SU07	Subh.	2.51	2.65	5.4	/	5386	2899	13.49
SU08	Reed	2.35	2.69	12.9	/	5386	2899	12.64
SU09	Reed	2.25	2.69	16.2	/	5408	2866	12.16
SU10	Reed	2.33	2.65	12.1	/	5364	2863	12.50
SU11	Reed	2.17	2.70	19.5	/	4942	2685	10.73
SU12	Reed	2.24	2.70	16.9	/	5217	2834	11.71
SU13	Subh.	2.56	2.66	3.8	/	5809	3091	14.89
SU14	Reed	2.20	2.68	17.8	/	4974	2714	10.95
SU15	Reed	2.33	2.68	13.3	/	5590	2976	13.01
SU16	Subh.	2.41	2.70	10.6	/	5335	2867	12.87
SU17	Subh.	2.32	2.70	14.0	/	5104	2759	11.86
SU18	Subh.	2.53	2.65	4.4	/	5739	3027	14.55
SU19	Subh.	2.53	2.67	5.2	/	5668	2996	14.36
SU20	Pook	2.52	2.69	6.5	/	5617	2933	14.15
SU21	Subh.	2.57	2.67	3.8	/	5580	3107	14.33
BU01	Subh.	2.32	2.67	13.2	0.1	5320	2883	12.33
BU02	Subh.	2.33	2.64	12.0	0.2	5409	2892	12.59
BU03	Subh.	2.33	2.67	12.7	0.1	5738	3010	13.39
BU04	Subh.	2.41	2.65	9.0	0.1	5569	2961	13.42
BU05	Casc.	2.39	2.66	10.1	0.1	5470	2899	13.07
BU06	Casc.	2.40	2.66	9.9	0.1	5345	2908	12.83
BU07	Casc.	2.43	2.66	8.4	0.1	5437	2942	13.22
BU09	Casc.	2.37	2.66	10.9	0.1	5195	2840	12.33
BU10	Casc.	2.26	2.66	15.0	0.8	5507	2917	12.47
BU11	Reed	2.19	2.68	18.1	7.0	5363	2834	11.75
BU12	Reed	2.29	2.66	14.1	412.1	6097	3140	13.94
BU13	Reed	2.43	2.66	8.4	0.5	5542	2982	13.49
BU14	Reed	2.12	2.66	20.3	19.2	5305	2840	11.26
BU15	Reed	2.38	2.65	10.0	0.4	5460	2897	13.01
BU16	Reed	2.32	2.67	12.8	3.4	5260	2816	12.23
BU18	Marl	2.46	2.66	7.5	3.1	5881	3020	14.44
BU19	Reed	2.08	2.68	22.4	18 000	5304	2792	11.02
BU20	Marl	2.43	2.65	8.2	23.8	5600	2980	13.63
BU21	Marl	2.49	2.65	5.9	/	5896	2941	14.69
BU23	Reed	1.97	2.68	26.4	/	5292	2668	10.44

Dry density (ρ_d). grain density (ρ_g). porosity (ø). Klinkenberg permeability (Kl. perm). p-wave velocity (V_p). s-wave velocity (V_s). Acoustic Impedance (A.I.). Sub-horizontal (subh.). Cascade (Casc.). Waterfall (Wfall.) facies.

were collected from three different locations, they all define one trend. The acoustic velocities are dependent on bulk densities (Kearey et al., 2002). Since there is hardly any change in the grain density of the samples, the bulk density is almost solely dependent on porosity. Therefore, compressional-wave, shear-wave velocity and porosity are expected to be inversely proportional. Both V_p and V_s show an increasing trend with decreasing porosity. Their correlation coefficients are 0.70 and 0.78, respectively.

When the samples are plotted according to their dominant pore type, it becomes clear that microporosity, interpeloidal and inter-laminar porosity plot below the regression line (Fig. 9). Mouldic pores are accompanied by an increase of P-wave velocities. Velocities in mouldic rocks are higher than for micro-mouldic rocks, which plot closer to the regression line. Samples dominated by vuggy pores plot above, on and below the regression line, while all 5 samples dominated by framework porosity yield low velocities and a negative departure from the average porosity−velocity path.
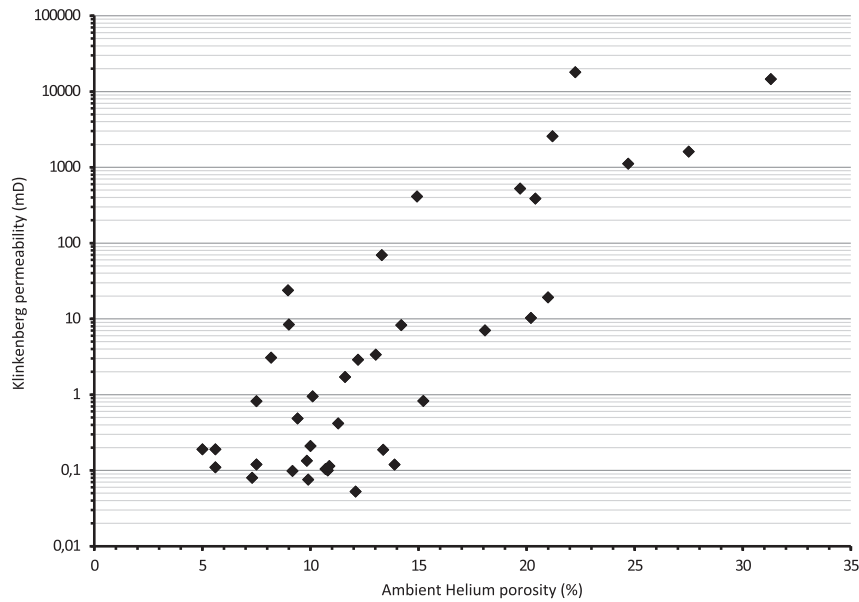
Figure 5. Cross plot of sample ambient Helium porosities and Klinkenberg permeabilities.

Samples with equal porosities, but different P-wave velocities are observed in the porosity - acoustic velocity plot. The scattering is caused by differences in pore types (Eberli et al., 2003). For example sample Al18 (with interlaminar porosity) has a total porosity of 20.2% and a V_p of 4703 m/s, while Al09 (with mouldic porosity) has a porosity that is very similar, 19.7%, but a V_p of 5253 m/s. Samples BU02 (with vuggy porosity) and Al08 (with mouldic porosity) also exhibit similar porosities, 12 and 12.9%, but different V_p values, 5409 and 5628 m/s, respectively. Three samples from Budakalász (BU12, BU19 and BU23) yield higher velocities than the other samples, with respect to their porosities. All three samples show an extensive cementation with sparitic, bladed crystals. The cementation causes a colour change from white-grey to orange-brown. In addition, sample BU23 underwent a later dissolution phase, increasing its total porosity when compared to other vuggy samples. Two other specimens (SU13 and SU18) are affected by cementation. However, these samples do not show increased velocities.

The elastic moduli of the samples (bulk, shear and Young's moduli, the Poisson's ratio, Lame constant and the acoustic impedance) can be calculated from the measured data. The Poisson's ratio is an elastic constant and a measure of the material compressibility perpendicular to the applied stress field. The ratio, used in seismic surveying as a diagnostic lithology indicator (Kearey et al., 2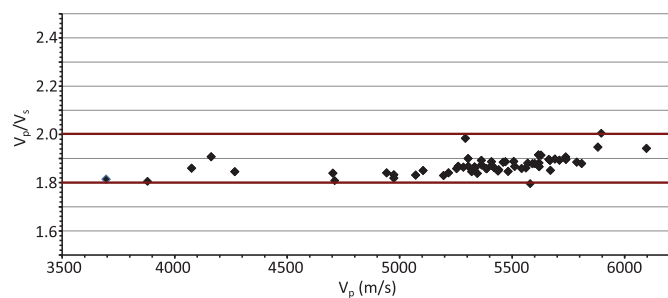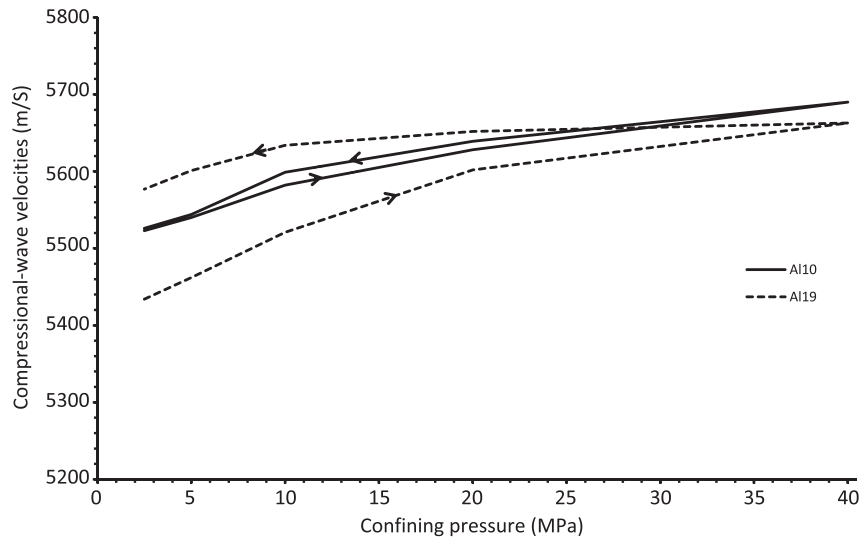002), ranges from 0.28 to 0.33 (with a mean value of 0.3). These results are typical for carbonate rocks, which always yield a Poisson's ratio around 0.3, compared to 0.2 for sandstones, above 0.3 for shales and 0.4 for coal lithologies (Schlumberger, 2013). The acoustic (or seismic) impedance of the medium in which body waves are travelling, is the product of the P-wave velocity and bulk density of the sample. Acoustic impedance differences will influence the reflection coefficient of the rocks. The observed range in P-wave velocities and dry bulk densities results in acoustic impedance contrasts, with values between 6.7 and 14.9×106 Ns/m^3. The acoustic impedance and porosity (Fig. 10) show an even better inversed correlation (0.91) than observed for Vp and porosity (0.70).

Compressional-wave velocities for the travertines are plotted along the Wyllie Time-Average (WTA) and Raymer−Hunt−Gardner (RHG) porosity-to-velocity transforms (Fig. 11). The transforms state that the total transit time is given by the sum of the transit times of the acoustic wave in the minerals and in the pore fluids (Mavko et al., 2009; Verwer et al., 2008). The WTA and RHG transforms were modelled for pure calcite compositions, with water as pore fluid. Gassmann's fluid-substitution equation was applied to predict the water saturated bulk modulus of the dry travertine samples and was used as input to calculate water saturated compressional-wave velocities. The saturated V_p values are higher than for the dry samples (7.5% on average, with a maximal surplus in velocity of 747 m/s). The measured velocities plot higher than predicted by the WTA and RHG equations. This is in agreement with earlier studies (Anselmetti and Eberli, 1993; Verwer et al., 2008), indicating that the WTA and RHG transforms predict averages for all sedimentary rock types, but require modifications towards higher velocities to predict reliable velocity-porosity couples in travertines. The Gassmann theory assumes that shear moduli remain constant during fluid substitutions. Baechle et al. (2005) as well as Adam et al. (2006) showed that this is not the case in carbonate rocks, which are in many cases affected by shear weakening and shear strengthening, limiting the applicability of Gassmann's theory for the velocity prediction in carbonates. The travertines in this study, however, are crystalline with a matrix regularly consisting of micritic peloids, bound by sparites. Crystalline rocks are expected to undergo shear strengthening, implying

Figure 6. V_p versus V_p/V_s ratio. For the entire V_p range, the V_p/V_s ratio ranges between 1.8 and 2.

Figure 7. Examples of hysteresis loops. Inflicted deformation by the applied confining pressures is considered elastic in sample Al10, where the hysteresis loop is closed, but non-elastic in sample Al19, where the hysteresis loop is open.

Gassmann underprediction (Verwer et al., 2008). If shear moduli would show non-constant behaviour, when applying fluid substitutions, than the actual acoustic velocities in these travertines are expected to exceed the WTA and RHG transforms even further.

4.5. Micro-Computer Tomography (μCT)

Ten representative samples were scanned with μCT to render the pore network in 3D. In addition to the petrographical subdivision into pore types, shape parameters were used to describe the pore network in artificial three-dimensional shapes. A pore type (Fig. 12A) is described by one of the given pore shapes (Fig. 12B). If

the ratio of the ellipsoid volume over the pore volume does not fall between 0.5 and 1.5, the pore is split op by a watershed algorithm. The best matching pore shape is assigned to the sub-pores (Fig. 12C). The results of the pore shape calculations are given in Table 2. Rod- and cuboid-like pore shapes are strongly elongated in 1 dimension. Cubic pores are equidimensional, while blade- and plate-like pore shapes have a strongly flattened appearance. The scanned samples were plotted in the porosity versus V_p graph, with the regression line of the entire dataset, to examine the influence of the pore shapes on body wave velocities (Fig. 13).

Rod- and cuboid-like pore shapes increase compressional-wave velocities. Samples dominated by rod- and/or cuboid-like pore shapes (>50vol%) are Al08, AL09 and BU11. They contain 85vol%,
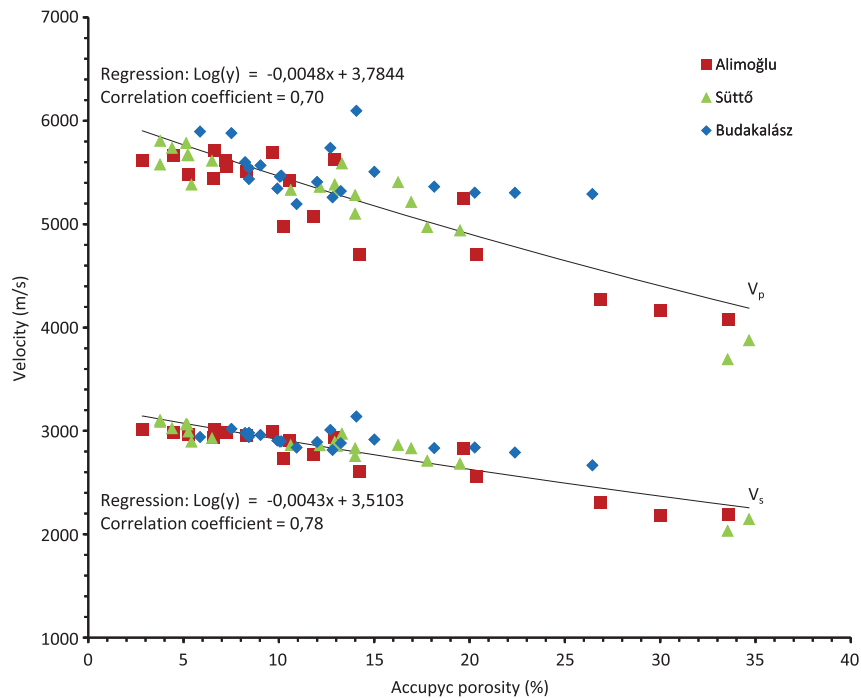
Figure 8. V_p and V_s versus sample porosities. Exponential, inversed trends are observed. Regression lines are provided.

8
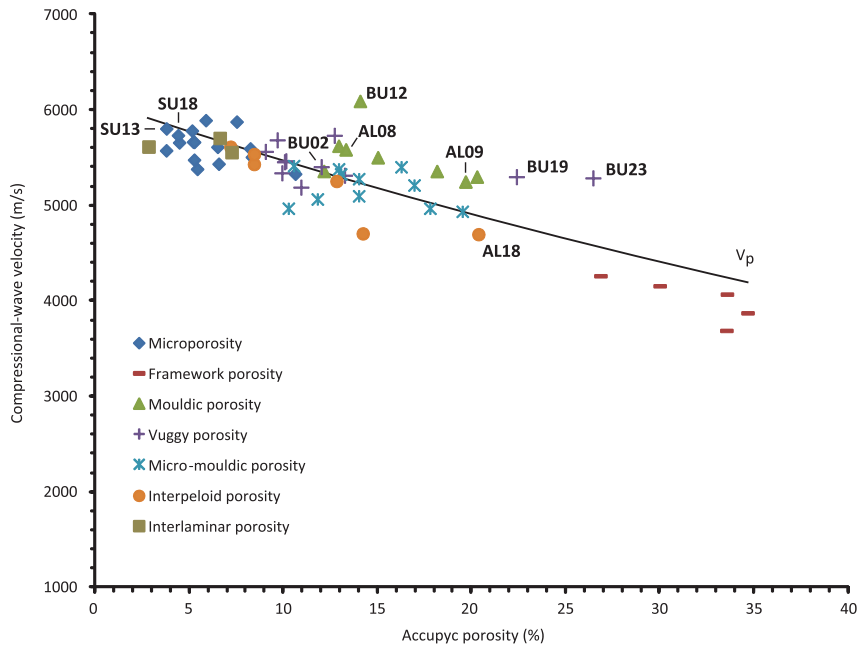
Figure 9. P-wave velocity versus porosity for the 7 dominant pore types in the travertine samples. The exponential trend line through the data is given as a reference. Velocity scatter at equal porosity is caused by the presence of different pore types in the samples.

89vol% and 58vol% rod- and cuboid-like pore shapes, respectively. These three samples plot above the regression line. Flattened pore shapes, i.e. plate- and blade-like pores, lower the acoustic wave propagation in travertines. Samples Al18 and SU18, with respectively 50vol% blade-like pores and 64vol% plate-like pores plot below the regression line. Equidimensional cubic pore shapes do not significantly increase or decrease compressional-wave propagation. Samples with elevated cubic pore volume percentages, as for example BU20, with 68vol% cubic-like pores, plot close to the regression line. The volume shares of the different pore shapes exert further control on acoustic velocities, additionally to the influence of pore types. Sample BU01, dominated by vuggy porosity, plots above the regression line, while sample BU06, also vug dominated, plots below it. BU01 contains 30% plate-like pores, 21%

cubic pores and 40% cuboid pore shapes. The amount of cuboid and cubic pore shapes is lowered in sample BU06, while the amount of plate-like pore shapes is increased. This change to more plate-like and less cuboid-like pore shapes in BU06 is probably the reason for its negative departure from the regression line. Similar observations can be made for microporous dominated samples (BU20, SU18 and Al19). BU20 contains for 68vol% cubic pores and low amounts of plate- and blade-like shapes. In SU18 and AL19, the blade- and plate-like shapes volume percentages are strongly increased. The latter flattened pore shapes explain why microporous samples SU18 and Al19 plot below the regression line.

Micro-focus CT scans (Fig. 14) of sample Al09 (porosity: 19.7%, V_p: 5253 m/s) and Al18 (porosity: 20.2%, V_p: 4703 m/s) revealed that their pore networks are significantly different. The 2D μCT
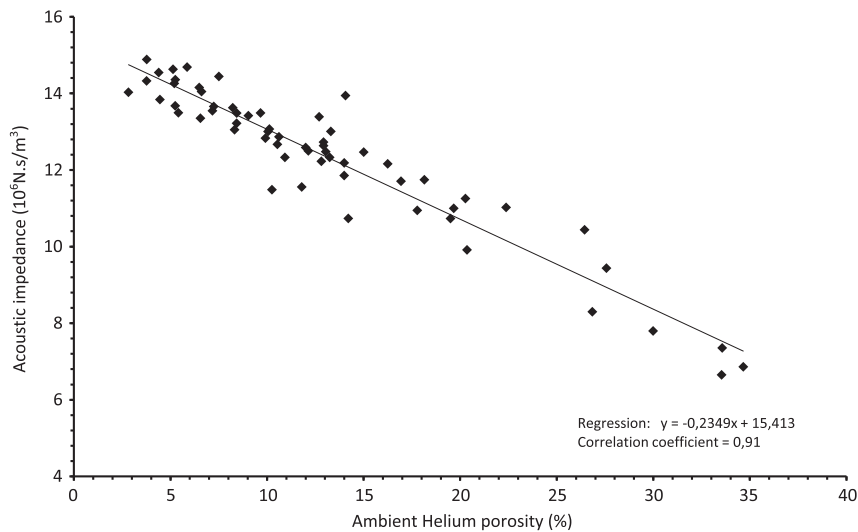
Figure 10. Acoustic Impedance and ambient Helium porosity, displaying a linear, inversed correlation.
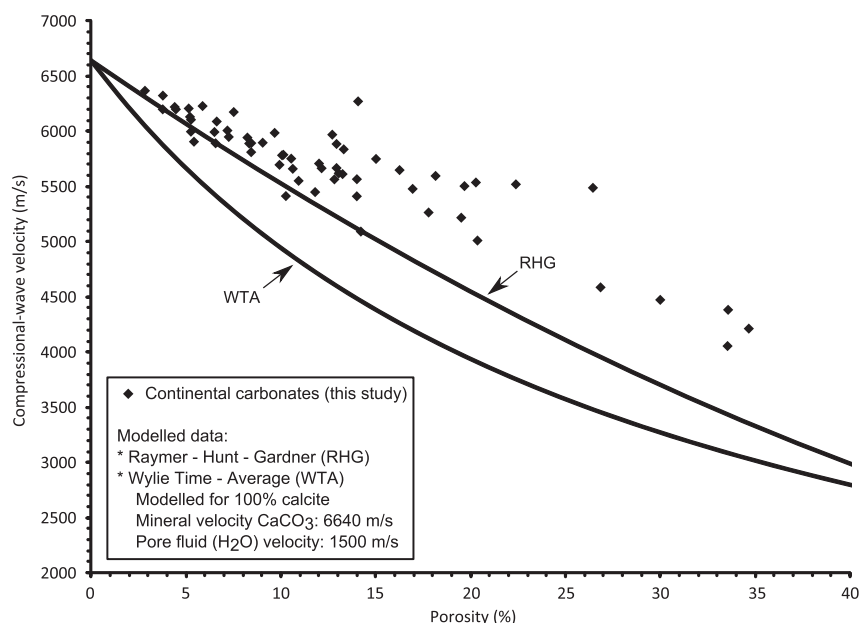
Figure 11. Porosity versus saturated compressional-wave velocities of the travertine data set. Superimposed are the WTA and RHG transforms calculated for a matrix velocity (calcite, $CaCO_3$) of 6640 m/s and a pore fluid velocity (H_2O) of 1500 m/s.
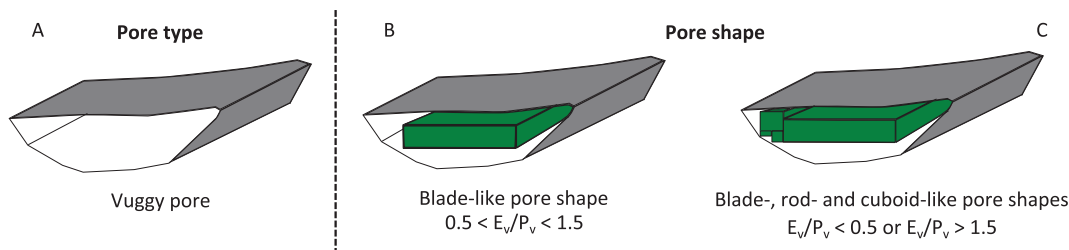
Figure 12. Artificial description of pore types into 3D pore shapes. (A) Sketch of a vuggy pore. (B) Blade-like pore shape filling the vuggy pore space. (C) The ratio of the ellipsoid volume and pore volume does not fall in between 0.5 and 1.5. A watershed algorithm divides up the pore and the best matching pore shape is assigned to the sub-pores.

slices show a dominance of oval shaped pores (average diameter of a few millimetres) in sample Al09 (Fig. 14A), compared to a dominance of more uniformly distributed oblate (micro-)pores in Al18, with a diameter of several 10s−100s of micrometres (Fig. 14B). A shell fragment can also be observed in the latter. Al09 is characterised by 86vol% cuboid-like pore shapes. This can be observed in the volume rendered and labelled pore network (Fig. 14C), where relict plant rods, running through the entire sample can be readily recognised. The oval shaped pores in the 2D slices are transects perpendicular to the length axis of the rods. In sample Al18, blade-,

cubic- and plate-like pores dominate the network (Fig. 14D). The smaller pore sizes in the latter require a larger quantity of pore objects to achieve similar porosities as for sample Al09. Hence, the porosity distribution is significantly different for both samples, patchy versus uniform respectively, implying that body waves will propagate in a different manner (Anselmetti and Eberli, 1993; Brigaud et al., 2010; Verwer et al., 2008).

5. Discussion

The travertines of this study exhibit large-scale ranges for both porosity and permeability. This is in line with expectations, given the petrographically observed (both on micro- and macroscale) heterogeneity of these limestones. The travertines in this study underwent a shallow burial history. The V_p/V_s ratio for all the samples varies between 1.8 and 2, which are values corresponding to indurated carbonates (Anselmetti and Eberli, 1993). This strongly suggests that artificial compaction was limited during the ultrasonic velocity analyses and that the travertine samples were strong enough to sustain the applied shear stresses. The travertines, even under limited burial conditions, can develop rigid rock frames that allow them, to a certain degree, to withstand compaction. Both V_p and V_s are reversely correlated with the sample porosity. The permeability is dependent on the porosity and connectivity between the individual pore bodies. However, no clear poro−perm

Table 2
Computer tomography pore shape calculations.

Sample number	Calculated pore shapes and their respective volumes (vol%)				
	Rod	Blade	Plate	Cube	Cuboid
AL08	35.88	3.84	5.48	5.2	49.53
AL09	2.58	1.05	3.13	6.72	86.49
AL13	9.85	2.56	30.24	34.13	23.36
AL18	23.45	49.85	7.02	3.99	15.63
AL19	10.74	20.73	24.14	14.42	29.91
BU01	3.69	4.4	30.11	21.72	39.99
BU06	5.96	4.75	43.48	15.84	29.88
BU11	31.94	2.84	9.84	28.82	26.55
BU20	11.71	2.63	4.97	68.14	12.52
SU18	7.42	4.42	64.47	9.94	13.71
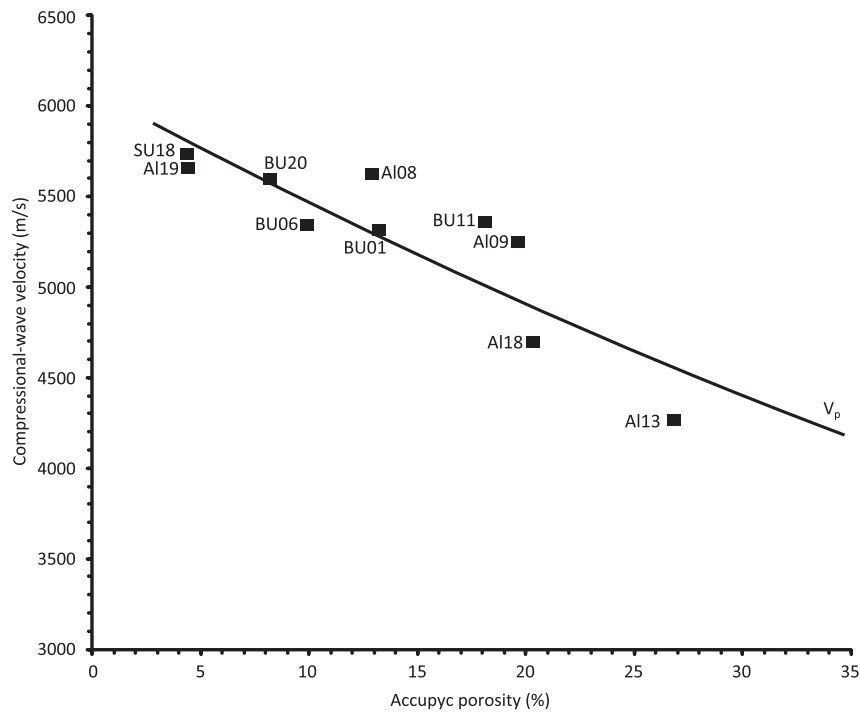
Figure 13. V_p plotted against porosity for the samples analysed with computer tomography. The regression line of all sixty samples is provided.

relation was found for these carbonates that exhibit complex texture and property distributions. The latter also make it difficult to understand relationships between seismic velocity and permeability. Factors that might influence the above mentioned relationships are the isotropic nature of porosity on the one hand and the anisotropic nature of permeability and acoustic velocity on the other hand. Saleh et al. (2008) found an apparent trend between shear-wave velocity and permeability in samples where velocity measurements were perpendicular to the direction of preferential permeability. The pore network tortuosity and complex flow paths in travertines, however, might hamper the observation of this trend. Experimental measurements are needed to unravel the acoustic velocity−permeability relationship.

Cementation results in more rigid self-supporting rock frames. Cements generally enhance the contact between individual crystals and building components throughout the sample. It will be these well-developed connections and the higher bulk modulus that facilitate acoustic wave propagation (Anselmetti and Eberli, 1993; Verwer et al., 2008). Low porosity samples (<10%) contain a primary, compact, dense and well-connected rock fabric, which easily transmits body waves. The stiffening effect of cements on the rock frame will therefore be limited. Connections between rock constituents in samples with higher porosities are less established and cements will connect the individual constituents. The accompanied increase of the bulk modulus will result in higher body wave velocities.

Travertine samples that exhibit similar porosities can have very distinct body wave propagation velocities. In siliciclastic rocks, this range would be explained by differences in sediment composition and associated mineralogy. The travertines in this study, however, consist almost exclusively of calcite, even aragonite was not retrieved in the XRD analysis. This means that either aragonite never precipitated, or that the pre-existing aragonite crystals underwent a complete transformation to calcite. The dominant calcite nature of these travertines suggests that factors, other than mineralogy, might be responsible for the differences in body wave

propagation velocities. Most likely fabric and texture of the travertines play an important role in the propagation speed of P- and S-waves (Anselmetti and Eberli, 1993; Verwer et al., 2008). With the limited diagenetic modifications and the strong porosity control on the compressional- and shear-wave velocities, pore morphologies and distributions may be important features to explain the velocity discrepancies.

μCT showed that samples with similar porosities but distinct P-wave velocities are significantly different. A compressional wave travelling through a sample will encounter pores. When the pores are uniformly distributed throughout the sample, more pore objects will be encountered by the wave, resulting in a scattered wave front. In samples where plant-mouldic pores predominate (for example Al09), a rigid, self-supporting micritic frame surrounds the sparite-reduced moulds. The rigid frame permits fast travel times for the wave front, with limited scatter. This frame-travelling time correlation explains why mouldic samples possess velocities that are higher than expected based on their total porosities (Anselmetti and Eberli, 1993). The observed difference in pore sizes, quantity of pore objects, shapes and their distribution results in the observed body-wave velocity discrepancies (Anselmetti and Eberli, 1993; Brigaud et al., 2010; Verwer et al., 2008).

The influence of pore types on the acoustic-wave velocity is also reported for marine carbonates. Dense, low porous samples generally plot close to the velocity known of pure calcites, 6260−6640 m/s (Mavko et al., 2009), similar velocities were reported for low porosity travertines in this study (Fig. 9). Fabric selective porosity types, such as microporosity, interpeloidal and interlaminar porosity in the travertines, tend to plot in the lower velocity area (Eberli et al., 2003). However, Weger et al. (2009) showed for various case studies that fabric selective pore types may plot over the entire velocity range. The velocity increase associated with mouldic porosity and the decrease associated with microporosity, as shown by various authors (Anselmetti and Eberli, 1993; Eberli et al., 2003; Fournier and Borgomano, 2007; Weger et al., 2009), agree with the findings of our study. The velocity

11
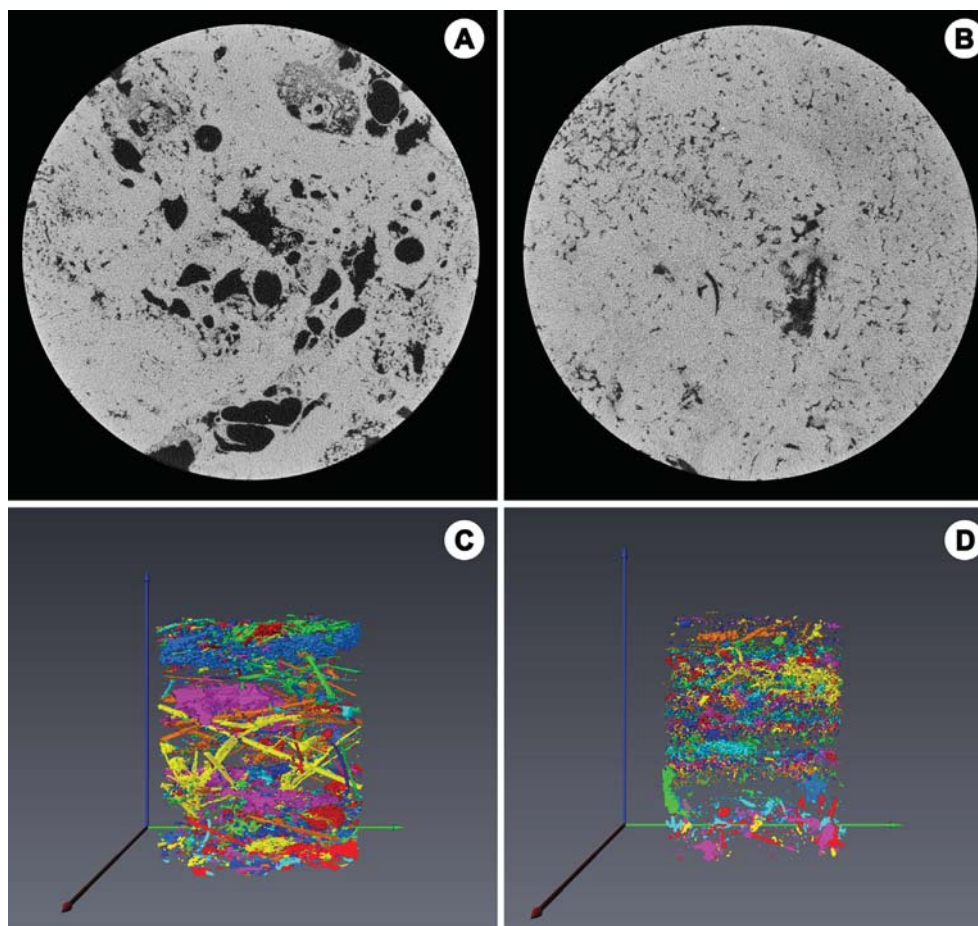
Figure 14. Slices and volume rendered pore networks, extracted from μCT scans. 2D slices perpendicular to the long axis of (A) sample Al09 and (B) sample Al18. (C) Dominance of cuboid and rod-like pore shapes in sample Al09. Plant casts, crosscutting the sample, are readily recognised. (D) Plate-like, cube and blade-like pores dominate in sample Al18. The portion of plant-mouldic pores is strongly reduced in this sample. The labelling, conducted on pore networks in C and D, assign the same colour code to connected pore bodies. (For interpretation of the references to colour in this figure legend, the reader is referred to the web version of this article.)

decrease is proportional to the percentage of micropores inside the sample. Weger et al. (2009) reported that large pores with simple pore structures, as for example the rod-like plant-mouldic pores (mm to several cm scale diameters), generally result in higher acoustic velocities. Vuggy pores in travertines can plot above, on or even below the regression line, since vuggy pores can vary greatly in size (μm to dm scale diameters) and shapes, giving rise to large specific pore surfaces. Framework porosity in this study is, in contrast to marine carbonates, associated with a lowering in velocity when compared to the general trend. The elastic rigidity of hollow encrusted reed stems, the framework builders in travertines, is lower than the rigidity of corals and bryozoans of a reefal growth framework (Eberli et al., 2003; Weger et al., 2009). This lower rigidity results in slower wave propagation. The pore network was described in artificial three-dimensional shapes by combining several shape parameters. The pore shapes exert further control on body wave velocities, in addition to the influence of pore types. Cuboid-and rod-like pore shapes increase the velocity, while plate-and blade-like pore shapes have a negative effect on the velocity. Samples with cubic pores plot close to the regression line. The 3D pore shapes allow understanding why for example a sample dominated by vuggy porosity shows a positive or negative departure from the regression line. A vuggy sample with high volume percentages of cuboid or rod-like pore shapes (BU01) will yield higher acoustic velocities than a vuggy sample with higher volume percentages of flattened pore shapes (BU06).

The comparison between acoustic velocities in travertines and in marine carbonates examined by Fournier et al. (2011, 2014) shows remarkable differences (Fig. 15). The data of Fournier et al. (2011) contains more than 70 tightly cemented Cretaceous carbonate grainstones from Provence (south-east France). The samples consist of calcite and are microporous (0.5−25.5%). 214 platform carbonates from SE France in Fournier et al. (2014) contain macroporosity and microporosity (0.1−23.1%). The travertines contain vast amounts of macropores and exhibit, just like macroporous marine carbonates (Fournier et al., 2014), higher velocities when compared to the microporous grainstones (Fournier et al., 2011). For porosities <12%, the travertines fall in a similar velocity range as mouldic, vuggy and intergranular macropores in marine carbonates (Fournier et al., 2014). At higher porosities, travertines yield higher velocities with respect to marine carbonates. Xu et al. (2009) calculated V_p in function of porosity and pore types (Fig. 16). Their model allows predicting pore type occurrences. The travertine dataset and the dataset from Fournier et al. (2011) are plotted alongside marine carbonates of Weger et al. (2009), Anselmetti and Eberli (1993) and Eberli et al. (2003). Figure 16 shows trend lines for compressional-wave velocities of the aforementioned datasets, in their respective porosity ranges.

12
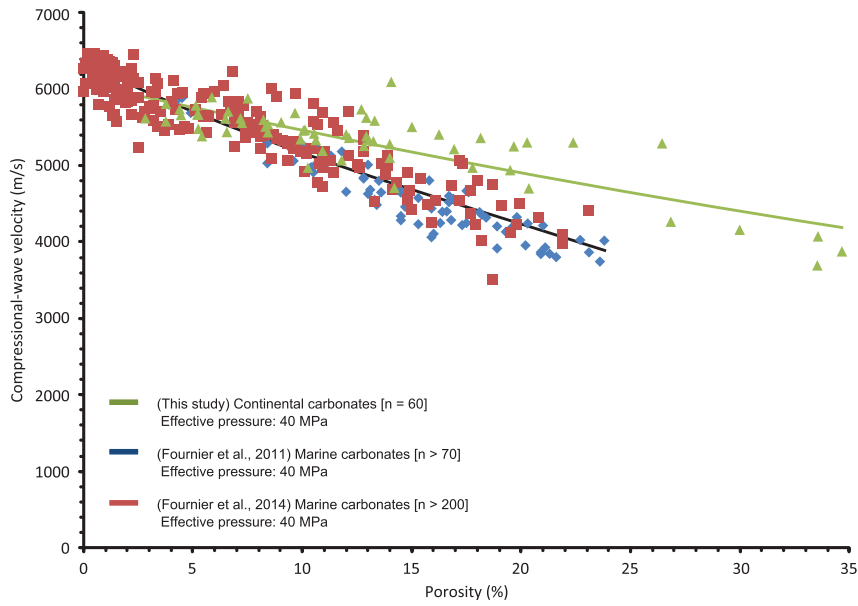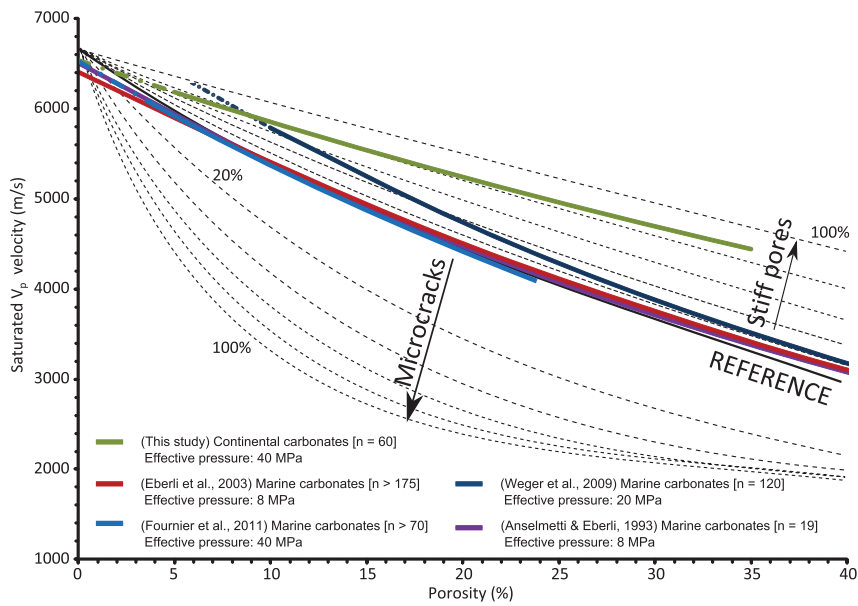
Figure 15. Porosity–acoustic velocity data for marine carbonates (Fournier et al., 2011), micro-and macroporous marine carbonates (Fournier et al., 2014) and continental carbonates. The trend line for the travertines and for all marine carbonate samples are given as a reference.

The dark blue trend line (Fig. 16) is based on 120 marine carbonate plugs (Weger et al., 2009). The samples originate from two drowned cool-subtropical platforms on the Marion Plateau (Miocene age) in Australia (Baechle et al., 2004), from the Shu'aiba Formation in the Middle East (Aptian age) and from an isolated carbonate platform (Miocene age) in Southeast Asia. The specimens are limestones, containing minor amounts of dolomite and less than 2% non-carbonate minerals. The porosity for these samples ranges between 8 and 45%. An inverse exponential correlation illustrates the relationship between sample porosity and compressional-wave velocities. The red trend line (Fig. 16) represents petrophysical data of Anselmetti and Eberli (1993) and

includes 190 marine carbonates. The samples originate from Montagna della Maiella in Abruzzi, Italy and from cores from the Great Bahama Bank. These sediments are calcite dominated and have a porosity range of 0–58%. The purple trend line (Fig. 16) is derived from Eberli et al. (2003), which are measurements of pure carbonate rocks from the Great Bahama Bank, ODP Site 1003, and Hole Unda, The Bahamas. These sediments exhibit porosities from 0 to 55%.

Despite the differences in porosity and mineralogy (dominantly calcite, but also dolomite and aragonite) in the marine carbonates, similar porosity–velocity relationships can be observed. The light blue trend line (Fournier et al., 2011), rich in micropores can be

Figure 16. Inverse porosity–acoustic velocity trend lines for marine (red, purple and blue lines) and continental (green line) carbonate lithologies, plotted in the model of Xu et al. (2009). Trend lines are extrapolated (dashed lines) outside the porosity ranges. (For interpretation of the references to colour in this figure legend, the reader is referred to the web version of this article.)

13

found directly underneath the reference line for limestones. The purple (Eberli et al., 2003) and red (Anselmetti and Eberli, 1993) trend lines contain in addition to the micropores also vugs, moulds and framework porosity. Both trend lines largely follow the limestone reference. The dark blue trend line (Weger et al., 2009) deviates from the other marine trend lines, moving further into the stiff pores area. The surplus in velocity (especially visible at lower porosities) is possibly related to the number of vug-dominated specimens in the 10−15% porosity range. Together with the reduced microporosity in this domain of the porosity-velocity cross plot, this can result in a shift of the trend line towards higher velocities. Generally, it seems that pure carbonate samples with similar porosities, but from different locations in the marine realm, come up with similar compressional-wave velocities.

The trend line for the travertines, however, defines a different path. With increasing porosity, the trend lines for marine carbonates and travertine diverge and V_p values in the latter become gradually higher than V_p values in marine carbonates with similar porosities. The travertine trend line exhibits a generally less steep slope and plots for almost the entire porosity range between the 80 and 100% stiff pore guidelines. Travertines produce porosity−velocity equations that significantly differ from those known for pure marine carbonates. The fabric and texture of the marine and continental limestones play a decisive role in the velocity differences. Travertines on the one hand are predominantly precipitates that form a rigid rock frame, often called framestone (Ford and Pedley, 1996; Özkul et al., 2010; Pedley, 2009), with large primary pores. Even at the surface or after minor burial they have considerable compressive and shear strength, as indicated by the high-pressure ultrasonic measurements. Marine carbonates on the other hand often consist of (cemented) transported sediments, resulting in a rock frame that permits slower wave propagation when compared to the continental limestones. Other differences that might influence wave velocities are the grain sizes and uniformity of the grain size distribution in marine carbonates versus crystal sizes (micrite and sparite) in travertines (Samsuri and Herianto, 2005; Wichtmann and Triantafyllidis, 2010).

6. Conclusion

The travertines in this study were subjected to a multi-technique approach (porosity, permeability, acoustic velocity and computer tomography analyses) that provides a more in depth understanding of these carbonates and their petrophysical properties.

Quaternary travertines from quarries in Denizli (Turkey) and from Süttő and Budakalász (Hungary) are petrophysically heterogeneous with porosities varying from 2.8 to 34.7% and permeabilities ranging between 0.05 and 18 000 mD. The heterogeneity results from a complex primary fabric, texture and pore type variability. The travertines are predominantly calcite. Despite the remarkably wide range of velocities in travertines (over 2400 m/s for V_p and 1100 m/s for V_s), the acoustic velocities of the samples that originate from three different locations, define one trend that clearly exhibits an inverse relation with sample porosity. The inverse relation is expected since the propagation of ultrasonic wave fronts is impeded in porous specimen. Shear wave velocities in a sample are approximately 50−55% of the compressional wave velocities, yielding V_p/V_s ratios of 1.8−2. These ratios are typical for all carbonates. The compressive strength of the rock frame ensures that porosity can be retained during burial and results in high reservoir potentials for these travertines.

Based on a petrographical analysis, specimens are subdivided into 7 dominant pore types: (1) microporosity, (2) interpeloidal porosity (3) interlaminar porosity, (4) mouldic porosity, (5) micro-mouldic porosity, (6) vuggy porosity and (7) framework porosity. Microporosity, interpeloidal and interlaminar porosity are associated with a negative acoustic velocity departure from the regression line. The increase in porosity that is associated with the appearance of mouldic and vuggy porosity partly blocks the propagation of the wave fronts. Micro-moulds have lower acoustic velocities, when compared to mouldic pores. The rigid frame in between the large moulds provides high velocity pathways for the wave fronts and results in acoustic velocities that are higher than expected from their porosities. Vugs can plot on, above or below the regression line. Diagenetic alterations, pedogenesis and primary framework porosity results in porosities exceeding 25%. Such high porosities impede the propagation of wave fronts even further. The compressional velocity in these samples is lowered to 3695−4267 m/s. The pore shapes exert further control on body wave velocities, in addition to the influence of pore types. Cuboid- and rod-like pore shapes increase the velocity, while plate-and blade-like pore shapes have a negative effect on the velocity. Samples with cubic pores plot close to the regression line.

The petrophysical analysis made clear that not the mineralogy, but the overall porosity, specific pore types, shapes and cementation influence the velocity of ultrasonic waves in travertine samples. Cementation has more effect on wave propagation in the highly porous samples ($\geq$15% porosity). This is illustrated by their positive departure from the best-fit curve. Low porosity samples have a compact nature, with interlocking crystals and touching particles in the sample matrix. Therefore, the rock frame stiffening by cementation will be limited and as a consequence, the bulk modulus will not increase as much as in highly porous samples, where they connect different rock fabric components.

Acoustic impedance data fall in between 6.7 and 14.9 (106 Ns/m^3). The range is caused by the variations in velocities and dry bulk densities. Seismic sections in mono-mineralic carbonate systems can contain seismic reflectors that are not caused by non-carbonate intercalations, but relate to geobody boundaries, in which the seismic expression is in function of porosity and pore types. The dependence of the acoustic impedance on the porosity is illustrated by the strong correlation between both parameters. The comparison of acoustic velocities in travertine rocks with those in pure, marine carbonates revealed that the travertine best-fit curve for porosity versus compressional-wave velocity follows a different trajectory. Body wave velocities in travertines show a slower velocity decrease with increasing porosity. This study provides petrophysical properties, i.e. ranges in porosity, permeability and acoustic velocities of travertines and is of high importance for the interpretation of seismic reflection data in subsurface continental carbonate reservoirs (Buckley et al., 2013).

References

Adam, L., Batzle, M., Brevik, I., 2006. Gassmann's fluid substitution and shear modulus variability in carbonates at laboratory seismic and ultrasonic frequencies. Geophysics 71 (6), F173–F183.

Alonso-Zarza, A.M., Tanner, L.H., 2010. Carbonates in Continental Settings, Facies, Environments and Processes. Elsevier.

Alçiçek, H., Varol, B., Özkul, M., 2007. Sedimentary facies, depositional environments and palaeogeographic evolution of the Neogene Denizli Basin, SW Anatolia, Turkey. Sediment. Geol. 202 (4), 596–637.

Anselmetti, F.S., Eberli, G.P., 1993. Controls on sonic velocity in carbonates. Pure Appl. Geophys. PAGEOPH 141 (2–4), 287–323.

Baechle, G., Weger, R., Eberli, G., Massaferro, J.L., 2004. The Role of Macroporosity and Microporosity in Constraining Uncertainties and in Relating Velocity to Permeability in Carbonate Rocks. In: Society of Exploration Geophysicists, Expanded Abstracts, 23.

Baechle, G., Weger, R., Eberli, G., 2005. Changes of shear moduli in carbonate rocks: implications for Gassmann applicability. Lead. Edge 507–510.

Bakacsi, Z.S., Mindszenty, A., Hertelendi, E., 1994. Lacustrine-palustrine facies from the Pleistocene Carbonate lake of Süttő (Hungary). In: IAS 15th Reg. Meeting, Ischia, Italy, Abstract, pp. 41–42.

Biot, M.A., 1956. Theory of propagation of elastic waves in a fluid-saturated porous solid, I. Low frequency range, II. Higher frequency range. J. Acoust. Soc. Am. 28, 168–191.

Blott, S.J., Pye, K., 2008. Particle shape: a review and new methods of characterization and classification. Sedimentology 55, 31–63.

Bozkurt, C., Bozkurt, E., 2009. Pattern of normal faulting in the Gediz Graben, SW Turkey. Tectonophysics 473 (1–2), 234–260.

Braaksma, H., Kenter, J.A.M., Proust, J.N., Dijkmans, V., Van Hoek, T., Mahieux, G., Drijkoningen, G.G., 2003. Case history controls on acoustic properties of Upper Jurassic siliciclastic rocks (Boulonnais, northern France). Geophysics 68 (1), 58–69.

Brigaud, B., Vincent, B., Durlet, C., Deconinck, J.-F., Blanc, N., Trouiller, A., 2010. Acoustic properties of ancient Shallow-Marine carbonates: effects of depositional environments and diagenetic processes (Middle Jurassic, Paris Basin, France). J. Sediment. Res. 80 (9), 791–807.

Bruker, 2013. DIFFRAC^{plus} EVA. Available at: http://www.bruker.com/products/x-ray-diffraction-and-elemental-analysis (accessed 22.08.13.).

Buckley, J.P., Elders, C., Mann, J., 2013. Carbonate Buildups in the Santos Basin, offshore Brazil. Programme and abstract volume: microbial carbonates in space and Time: implications for global exploration and production. Geol. Soc. Lond. 37–39.

Choquette, P., Pray, L., 1970. Geologic nomenclature and classification of porosity in sedimentary carbonates. AAPG Bull. (2), 207–250.

Claes, H., Soete, J., El Desouky, H.A., Van Noten, K., Özkul, M., Swennen, R., 2014. 3D geobody reconstruction and CO$_2$-origin of Pleistocene travertine deposits in the Ballık area (SW Turkey). Sedimentology (submitted for puclication).

Claes, S., Soete, J., Claes, H., Swennen, R., 2013. 3D Visualization and Quantification of the Porosity Network in Travertine Rocks. The Geological Society, London, pp. 79–81.

Coelho Software, 2012. TOPAS-academic V4.1. Available at: http://www.topas-academic.net/ (accessed 15.08.13.).

Dewit, J., Huysmans, M., Muchez, P., Hunt, D.W., Thurmond, J.B., Verges, J., Saura, E., Fernandez, N., Romaire, I., Esestime, P., Swennen, R., 2012. Reservoir characteristics of fault-controlled hydrothermal dolomite bodies: Ramales Platform case study. Geol. Soc. Lond. Special Publications 370 (1), 83–109.

Dolton, G., 2006. Pannonian Basin Province, Central Europe (Province 4808)-Petroleum Geology, Total Petroleum Systems and Petroleum Resource Assessment. USGS (Province 4808).

Eberli, G., Baechle, G., Anselmetti, F., Incze, M., 2003. Factors controlling elastic properties in carbonate sediments and rocks. Lead. Edge 654–660.

El Desouky, H.A., Soete, J., Claes, H., Özkul, M., Vanhaecke, F., Swennen, R., 2014. Genesis of the Ballık travertines, Denizli Basin, Western Turkey: evidence from fluid inclusions and isotope geochemistry. Sedimentology.

Flügel, E., 2010. Microfacies of Carbonate Rocks, second ed. Springer-Verlag.

Ford, T.D., Pedley, H.M., 1996. A review of tufa and travertine deposits of the world. Earth-Sci. Rev. 41 (3–4), 117–175.

Fouke, B.W., 2011. Hot-spring Systems Geobiology: abiotic and biotic influences on travertine formation at Mammoth Hot Springs, Yellowstone National Park, USA. Sedimentology 58 (1), 170–219.

Fournier, F., Borgomano, J., 2007. Geological significance of seismic reflections and imaging of the reservoir architecture in the Malampaya gas field (Philippines). AAPG Bull. 91 (2), 235–258.

Fournier, F., Leonide, P., Biscarrat, K., 2011. Elastic properties of microporous cemented grainstones. Geophysics 76 (6), E211–E226.

Fournier, F., Léonide, P., Kleipool, L., Toullec, R., Reijmer, J.J.G., Borgomano, J., Klootwijk, T., Van Der Molen, J., 2014. Pore space evolution and elastic properties of platform carbonates (Urgonian limestone, Barremian–Aptian, SE France). Sediment. Geol. 308, 1–17.

García-del-Cura, M.Á., Benavente, D., Martínez-Martínez, J., Cueto, N., 2012. Sedimentary structures and physical properties of travertine and carbonate tufa building stone. Constr. Build. Mater. 28 (1), 456–467.

Gassmann, F., 1951. Elastic waves through a packing of spheres. Geophysics 16, 673–685.

Goldscheider, N., Mádl-Szőnyi, J., Erőss, A., Schill, E., 2010. Review: thermal water resources in carbonate rock aquifers. Hydrogeol. J. 18 (6), 1303–1318.

Gündoğan, I., Helvacı, C., Sözbilir, H., 2008. Gypsiferous carbonates at Honaz Dağı (Denizli): first documentation of Triassic gypsum in western Turkey and its tectonic significance. J. Asian Earth Sci. 32 (1), 49–65.

Guo, L., Riding, R., 1998. Hot-spring travertine facies and sequences, Late Pleistocene, Rapolano Terme, Italy. Sedimentology 45 (1), 163–180.

Gürbüz, A., Boyraz, S., Ismael, M.T., 2012. Plio-Quaternary development of the Baklan–Dinar graben: implications for cross-graben formation in SW Turkey. Int. Geol. Rev. 54 (1), 33–50.

Gürer, Ö.F., Yilmaz, Y., 2002. Geology of the Ören and surrounding areas, SW Anatolia. Turkish J. Earth Sci. 11, 1–13.

Haas, J., 2012. Influence of global, regional, and local factors on the genesis of the Jurassic manganese ore formation in the Transdanubian Range, Hungary. Ore Geol. Rev. 47, 77–86.

Kearey, P., Brooks, M., Hill, I., 2002. An Introduction to Geophysical Exploration. Blackwell Publishing.

Kele, S., 2009. Investigations on Freshwater Limetones from the Carpathian-basin: Paleoclimatological and Sedimentological Studies (in Hungarian). Ph.D. thesis. Eötvös University, Budapest.

Kele, S., Vaselli, O., Szabó, C., Minissale, A., 2003. Stable isotope geochemistry of Pleistocene travertine from Budakalász (Buda Mts., Hungary). Acta Geol. Hung. 46 (2), 161–171.

Kele, S., Özkul, M., Fórizs, I., Gökgöz, A., Baykara, M.O., Alçiçek, M.C., Németh, T., 2011. Stable isotope geochemical study of Pamukkale travertines: new evidences of low-temperature non-equilibrium calcite-water fractionation. Sediment. Geol. 238 (1–2), 191–212.

Kenter, J.A.M., Fouke, B.W., Reinders, M., 1997. Effects of differential cementation on the sonic velocities of Upper Cretaceous skeletal grainstones (southeastern Netherlands). J. Sediment. Res. 67 (1), 178–185.

Khatib, S., Rochette, P., Alçiçek, M.C., Lebatard, A.-E., Demory, F., Saos, T., 2014. Études stratigraphique, sédimentologique et paléomagnétique des travertins de Kocabaş, Bassin de Denizli, Anatolie, Turquie, contenant des restes fossiles quaternaires. L'Anthropologie 118 (1), 16–33.

Lapponi, F., Casini, G., Sharp, I., Blendinger, W., Fernandez, N., Romaire, I., Hunt, D., 2011. From outcrop to 3D modelling: a case study of a dolomitized carbonate reservoir, Zagros Mountains, Iran. Pet. Geosci. 17 (3), 283–307.

Lønøy, A., 2006. Making sense of carbonate pore systems. AAPG Bull. 90 (9), 1381–1405.

Mavko, G., Mukerji, T., Dvorkin, J., 2009. The Rock Physics Handbook, second ed. Cambridge.

Nador, A., 1993. Paleokarsts and Long-term Karst Evolution of the Buda Mountains, Hungary. Bulletin de la Societe Geographique de Liège, pp. 139–143.

Nurmi, R., Standen, E., 1997. Carbonates, the inside story. Middle East Well Eval. Rev. 18, 28–41.

Özkul, M., Varol, B., Alçiçek, M.C., 2002. Depositional environments and petrography of denizli travertines. Mineral. Res. Expl. Bul. 125, 13–29.

Özkul, M., Gökgöz, A., Horvatinčić, N., 2010. Depositional properties and geochemistry of Holocene perched springline tufa deposits and associated spring waters: a case study from the Denizli Province, Western Turkey. Geol. Soc. Lond. Special Publications 336 (1), 245–262.

Özkul, M., Kele, S., Gökgöz, A., Shen, C.-C., Jones, B., Baykara, M.O., Fórizs, I., Németh, T., Chang, Y.-W., Alçiçek, M.C., 2013. Comparison of the quaternary travertine sites in the Denizli extensional basin based on their depositional and geochemical data. Sediment. Geol. 294, 179–204.

Özkul, M., Gökgöz, A., Kele, S., Baykara, M.O., Shen, C.-C., Chang, Y.-W., Kaya, A., Hançer, M., Aratman, Cï., Akin, T., Örü, Z., 2014. Sedimentological and geochemical characteristics of a fluvial travertine: a case from the eastern Mediterranean region. E. Capezzuoli, ed. Sedimentology 61 (1), 291–318.

Pedley, M., 2009. Tufas and travertines of the Mediterranean region: a testing ground for freshwater carbonate concepts and developments. Sedimentology 56 (1), 221–246.

Pedley, H.M., Rogerson, M., 2010. Tufas and Speleothems Unravelling the Microbial and Physical Controls. Geological Society.

Pentecost, A., 2005. Travertine. Geologist Association, Springer.

Roduit, N., 2002-2007. JMicroVision: Image Analysis Toolbox for Measuring and Quantifying Components of High-definition Images. Version 1.27. http://www.jmicrovision.com (accessed 23.10.13.).

Saleh, M., Prasad, M., Vega, S., Sharma, R., 2008. A Study of Permeability and Velocity Anisotropy in Carbonates. The Petroleum Institute, pp. 1–9.

Samsuri, A., Herianto, H., 2005. The effect of grain size distributions on acoutic wave velocities in porous rocks. In: 8th. International Conference on Quality in Research (QIR), University Indonesia, Jakarta, Indonesia.

Schlumberger Limited, 2013. Oilfield Glossary, the Poisson's Ratio. Available at: http://www.glossary.oilfield.slb.com/en/terms/p/poissons_ratio.aspx (accessed 22.07.13.).

Sierralta, M., Kele, S., Melcher, F., Hambach, U., Reinders, J., van Geldern, R., Frechen, M., 2010. Uranium-series dating of travertine from Süttő: implications for reconstruction of environmental change in Hungary. Quat. Int. 222 (1–2), 178–193.

Thompson, L., Oftebro, C., 2011. Salt gets in your eyes: the geological challenges and solutions to sub-salt exploration. Image (Rochester, N.Y.) 29 (March), 93–98.

Toumelin, E., Chen, S., Fischer, D.M., 2003. Reconciling NMR measurements and numerical simulations: assessment of temperature and diffusive coupling effects on two-phase carbonate samples 1. Petrophysics 44 (2), 91–107.

Van Noten, K., Claes, H., Soete, J., Foubert, A., Özkul, M., Swennen, R., 2013. Fracture networks and strike–slip deformation along reactivated normal faults in Quaternary travertine deposits, Denizli Basin, western Turkey. Tectonophysics 588, 154–170.

Verwer, K., Braaksma, H., Kenter, J.A.M., 2008. Case history acoustic properties of carbonates: effects of rock texture and implications for fluid substitution. Geophysics 73 (2), B51–B65.

Wang, Z., Hirsche, W.K., Sedgwick, G., 1991. Seismic velocities in carbonate rocks. Can. Pet. Tech. 30, 112–122.

Weger, R.J., Eberli, G.P., Baechle, G.T., Massaferro, J.L., Sun, Y.-F., 2009. Quantification of pore structure and its effect on sonic velocity and permeability in carbonates. AAPG Bull. 93 (10), 1297–1317.

Wichtmann, T., Triantafyllidis, T., 2010. On the influence of the grain size distribution curve on P-wave velocity, constrained elastic modulus M max and Poisson's ratio of quartz sands. Soil Dyn. Earthq. Eng. 30 (8), 757–766.

Wright, V.P., 2012. Lacustrine carbonates in rift settings: the interaction of volcanic and microbial processes on carbonate deposition. Geol. Soc. Lond. Special Publications 370 (1), 39–47.

Xu, S., Payne, M., Exxonmobil, 2009. modeling elastic properties in carbonate rocks. Lead. Edge 66–74.